Article

ZnSnO$_3$ or Zn$_2$SnO$_4$/SnO$_2$ Hierarchical Material? Insight into the Formation of ZnSn(OH)$_6$ Derived Oxides

Davide Redolfi-Bristol [1], Lorenzo Branzi [1], Michele Back [1], Pietro Riello [1], Adolfo Speghini [2], Nicola Pinna [3] and Alvise Benedetti [1,*]

[1] Dipartimento di Scienze Molecolari e Nanosistemi, Università Ca' Foscari Venezia, Via Torino 155, Venezia Mestre, 30172 Venice, Italy

[2] Nanomaterials Research Group, Department of Biotechnology and INSTM, RU Verona, University of Verona, Strada le Grazie 15, 37134 Verona, Italy

[3] Institut für Chemie and IRIS Adlershof, Humboldt-Universität zu Berlin, Brook-Taylor-Str. 2, 12489 Berlin, Germany

* Correspondence: benedett@unive.it

Abstract: Piezoelectric materials are a class of compounds that is gaining increasing interest in various applications such as energy harvesting. During the last decade, lead-free ZnSnO$_3$ perovskite ceramic has gained attention among the scientific community thanks to its unique symmetry-dependent and spontaneous polarization properties such as piezoelectricity and ferroelectricity. Nevertheless, only a few studies successfully prepared pure ZnSnO$_3$, while most seem to mislead the product for its hydroxide precursor (ZnSn(OH)$_6$) or a mixture of Zn$_2$SnO$_4$ and SnO$_2$. In our work, we investigated the conversion of ZnSn(OH)$_6$ at different temperatures (500, 600, 700, 750 and 800 °C) by X-ray powder diffraction analysis, and in-situ using synchrotron radiation up to 950 °C under ambient atmosphere and in a vacuum, to reproduce conventional reaction conditions. SEM and TEM have been used to understand the evolution of the particle shape and surface structure before and after the thermal treatments. Our results show the instability of the ZnSn(OH)$_6$ phase, which converts into an amorphous structure at low temperature. Above 750 °C, the material segregates into Zn$_2$SnO$_4$ and SnO$_2$, supporting the hypothesis that the thermal treatment of the hydroxide phase under typical conditions results in the formation of an oxide mixture rather than the phase pure ZnSnO$_3$.

Keywords: crystal structure; materials; phase transitions; zinc stannate

1. Introduction

Piezoelectricity (also called piezoelectric effect) is the phenomenon whereby specific materials are electrically polarized as a result of mechanical deformation of elastic nature (direct piezoelectric effect), and vice versa are elastically deformed when subjected to the action of an electric field (inverse piezoelectric effect) [1]. The piezoelectric effect is at the basis of various applications especially in pressure sensors (largely employed in the automobile industry), ultrasound scanners in medical diagnosis, microphones, etc [2–4]. In recent years, piezoelectricity has also been exploited in emerging technologies like Kinematic Energy Harvesting Devices, which intend to convert mechanical stimuli into electrical energy to be stored or used to power small devices [5,6]. The growing interest in piezoelectricity has led researchers to investigate new and more efficient materials to be used in required fields of application [7,8]. The perovskite solid solution Pb[Zr$_x$Ti$_{1-x}$]O$_3$ (PZT), which exhibits some of the highest polarization and piezoelectric outcomes [9–11], is the crystalline system generally recognized as the most piezoelectrically performing. Indeed, for many years PZT ceramics have been the pillar material for piezoelectric actuators, sensors, microphones, etc [12–14]. Nevertheless, due to the toxicity of lead, new materials have been searched for and studied to meet environmental and health needs [15]. Some remarkable examples of lead-free piezoelectric materials widely considered promising candidates for potential

application include different oxide perovskites such as $BaTiO_3$ [16–18], $NaNbO_3$ [19–21] and $LiNbO_3$ [22–24] to name a few.

In the past decade, several efforts have been made to investigate $ZnSnO_3$, an *R3c* $LiNbO_3$-type perovskite ceramic. This lead-free piezoelectric system has gained large interest among the scientific community due to its unique symmetry-dependent and spontaneous polarization properties such as piezoelectricity, ferroelectricity, pyroelectricity, and second-order non-linear optical behavior [25–29]. Son et al. [27] reported high ferroelectric polarization of 47 $\mu C/cm^2$ in an epitaxially grown $ZnSnO_3$ thin film, which makes it an appealing material in the ferroelectric application. Among the promising properties observed for $ZnSnO_3$ crystals, other characteristics of this material, such as the supposed facile production by earth-abundant minerals, have stimulated several works and several methods to prepare $ZnSnO_3$ perovskite phase, also in an easy way, through solid-state reaction method [30], sol-gel method [31,32], precipitation method [33,34], electrospinning method [35,36] or hydrothermal methods [37–39]. However, a detailed characterization of the crystalline structure is usually missing. The supporting powder X-Ray Diffractions (PXRD) data refer to $ZnSn(OH)_6$ precursor [33,34,37,39] or to a mixture of Zn_2SnO_4 and SnO_2 [30–32,35,36,38] and not to phase pure $ZnSnO_3$. This framework is further complicated by the large use of misleading references for qualitative phase identification. In fact, the XRD patterns are generally compared to the ICDD PDF No. 11-0274 or 28-1486 which instead correspond to $ZnSn(OH)_6$ and to the mixture of Zn_2SnO_4 and SnO_2, respectively (PDF No. 28-1486 has been deleted from the ICDD database) [25]. Moreover, the morphological differences of the reported materials make the interpretation of this system even more complex. Up to now, only two previous investigations describe the successful preparation of single phase $ZnSnO_3$: one is focused on using ion exchange reaction forming ilmenite-$ZnSnO_3$ [40], and the other describes a high-pressure method to form perovskite structure of $ZnSnO_3$ [26]. The latter paper shows excellent crystallinity and the respective PDF is the basis of most of the subsequent works. Few other studies report the preparation of $ZnSnO_3$ through pulsed laser deposition [27,29] or hydrothermal method [28], however never as a single-phase material. So far a detailed in-situ analysis of the crystalline and morphological evolution of $ZnSn(OH)_6$ into $ZnSnO_3$ and Zn_2SnO_4/SnO_2 with temperature is still missing. This fact leads still to a great ambiguity in the interpretation of the structural characteristics and the relative properties outcomes. In fact, it is important to point out that $ZnSn(OH)_6$, Zn_2SnO_4, and SnO_2 present a centrosymmetric crystal structure which, from a theoretical point of view, should not exhibit piezoelectric properties based on simple lattice distortion under mechanical stress [41]. The observed piezoelectric properties reported by several articles could be associated with the effect of symmetry breaking in a certain portion of the material (particle or composite). Recent observations have shown that the application of a specific stimulus such as static electric fields [42] or the potential generated by a Schottky junction [43] can lead to a local symmetry breaking, this kind of process has recently stimulated a large interest in the pursuit to induce piezoelectricity and other properties in centrosymmetric structures.

In the present study, we investigated the effects of the calcination process on $ZnSn(OH)_6$ prepared via the reflux method at different temperatures (500, 600, and 750 °C) by X-ray powder diffraction (XRPD) analysis. In addition, we monitored in-situ the evolution of $ZnSn(OH)_6$ using synchrotron radiation up to 950 °C under an ambient atmosphere and in a vacuum, to reproduce typical conditions employed. Our results reveal an instability of the hydroxide-based phase, which undergoes the formation of an amorphous structure under heat treatment. At high temperatures, the segregation into SnO_2 and Zn_2SnO_4 is observed, confirming the hypothesis that, close to ambient pressure, the thermal treatment of the hydroxide phase leads to the formation of an oxide mixture rather than the $ZnSnO_3$ perovskite. Thermogravimetric differential scanning calorimetry analysis (TG-DSC) was also employed to further investigate the phase progression, showing the decomposition of $ZnSn(OH)_6$ into Zn_2SnO_4/SnO_2 and never revealing the formation of $ZnSnO_3$ as intermediate. Scanning electron microscopy (SEM) and transmission electron microscopy

(TEM) has been also extensively used to elucidate novel details on the evolution of the particle shape and surface structure after the thermal treatments, confirming the formation of Zn_2SnO_4/SnO_2 hierarchically structured material.

2. Results

ZnSn(OH)$_6$ microcrystals are prepared by refluxing an alkaline solution of zinc acetate and tin tetrachloride for 1.0 h. The chemical reaction is represented in Scheme 1. As shown in Figure 1 the process forms particles with well-defined cubic morphology and an average size of around 1.6 µm (Figure S1). The XRD pattern confirms the expected structure of the hydroxide phase ZnSn(OH)$_6$ (space group Pn-3) Figure S2.

$$Zn(OAc)_2 + SnCl_4 \xrightarrow[\text{1 h reflux}]{\text{6 NaOH}} ZnSn(OH)_6 + 4\ NaCl + 2\ AcONa$$
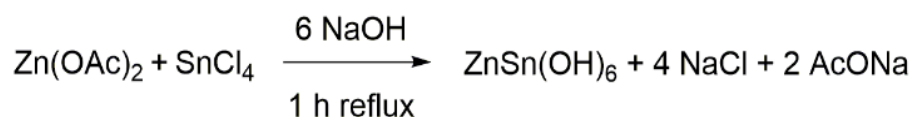
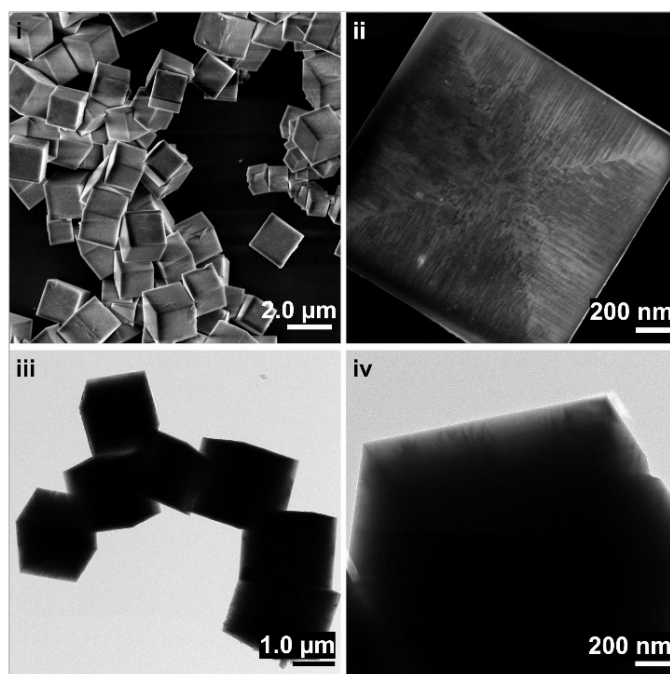**Scheme 1.** Synthesis of ZnSn(OH)$_6$ microcubes.

Figure 1. (**i**), ii SEM and iii, iv TEM images of the ZnSn(OH)6 particles produced by reflux treatment. The scale bars correspond to (**i**) = 2000, (**ii**) = 200, (**iii**) = 1000 and (**iv**) = 200 nm.

After the synthesis, the hydroxide particles were converted to oxides by a post-synthetic calcination step. For this purpose, the ZnSn(OH)$_6$ phase was heat treated at 500, 600, 700, 750, and 800 °C respectively and for 2.0 h under ambient atmosphere, followed by a thermal quenching at room temperature. The XRD analyses of the samples (shown in Figure 2) reveal significant structural modifications. The diffraction data show the presence of SnO$_2$ phase for samples treated at 500 and 600 °C, evidenced by broad diffraction peaks around 26.4, 33.8, and 51.8 degrees that can be assigned to the 110, 101, and 002 planes respectively. Moreover, the contribution to the background can be ascribed to a large content of an amorphous phase. Instead, the samples treated at 700, 750, and 800 °C show two distinct crystalline phases that can be related to SnO$_2$ rutile and Zn$_2$SnO$_4$ spinel crystal structures respectively (Figure S3).
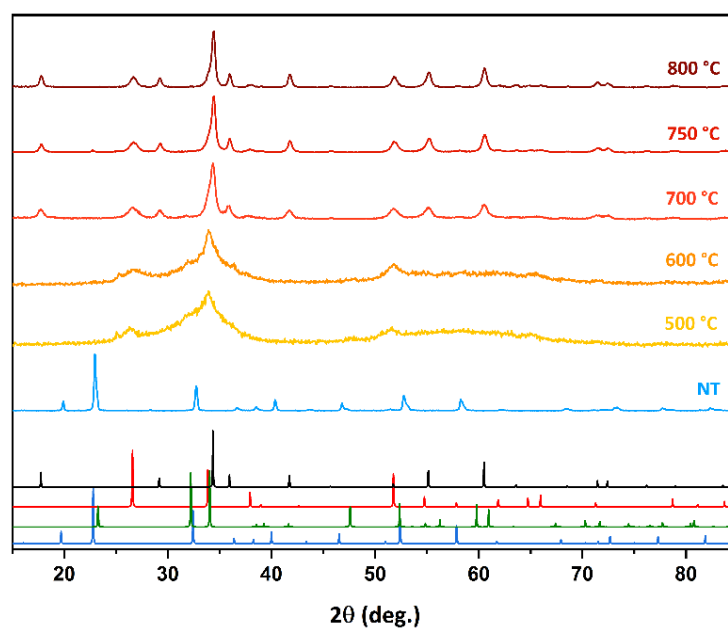
Figure 2. XRD patterns of the particles after the different treatments; NT: $ZnSn(OH)_6$ not-treated. The reference diffraction patterns correspond respectively to: blue $ZnSn(OH)_6$ (ICSD 27767), green $ZnSnO_3$ (ICSD 245943), red SnO_2 (ICSD 9163) and black Zn_2SnO_4 (ICSD 11269).

These observations agree with the conclusions reported by others groups that investigated the thermal evolution of the $ZnSn(OH)_6$ structure [44–46].

In order to study in detail the thermal crystallographic evolution of the $ZnSn(OH)_6$ phase, some in-situ XRD analyses were performed at variable temperatures up to 950 °C and at different time intervals at 600 °C. The aims of these experiments are: (i) to collect in-situ evidence on the evolution of the crystallographic structure with high resolution, in conditions that are conventionally employed in laboratory furnaces for the post-synthetic calcination treatments, (ii) to support the hypothesis of the production of the mixed oxide phase by the thermal treatment at relatively low pressure, and (iii) collect possible information about the formation of metastable phases not directly observable after thermal quenching.

2.1. Air Flux Condition

Figure 3i reports the XRD patterns of the sample treated from 30 to 950 °C under air flux and with a heating rate of 10 °C/min. The analysis evidence that the $ZnSn(OH)_6$ crystal structure is stable up to 250 °C while at higher temperatures the hydroxide decomposes into an amorphous phase. It is therefore most probably that the crystal structure of $ZnSn(OH)_6$ undergoes a structural change due to the elimination of water molecules according to the reaction Scheme 2 R.1, leading to the formation of a highly disordered structure. Increasing the temperature to 700 °C, the formation of SnO_2 nanocrystals is confirmed by the presence of the 110 and 101 reflections, meanwhile, at higher temperatures, the formation of the Zn_2SnO_4 phase is observed according to reaction Scheme 2 R.1. These results are also confirmed by TG-DSC analysis performed on $ZnSn(OH)_6$ microcubes from 25 to 900 °C under the same air conditions and heating rate (Figure S4). In the DSC curve, it can be observed a sharp endothermic peak at 260 °C corresponds to the release of water molecules from $ZnSn(OH)_6$. This peak correctly matches the 18% weight loss shown in the TG curve in the same region. The exothermic peak at 730 °C has instead related to the decomposition of the amorphous phase into a crystalline SnO_2 and Zn_2SnO_4 mixture.
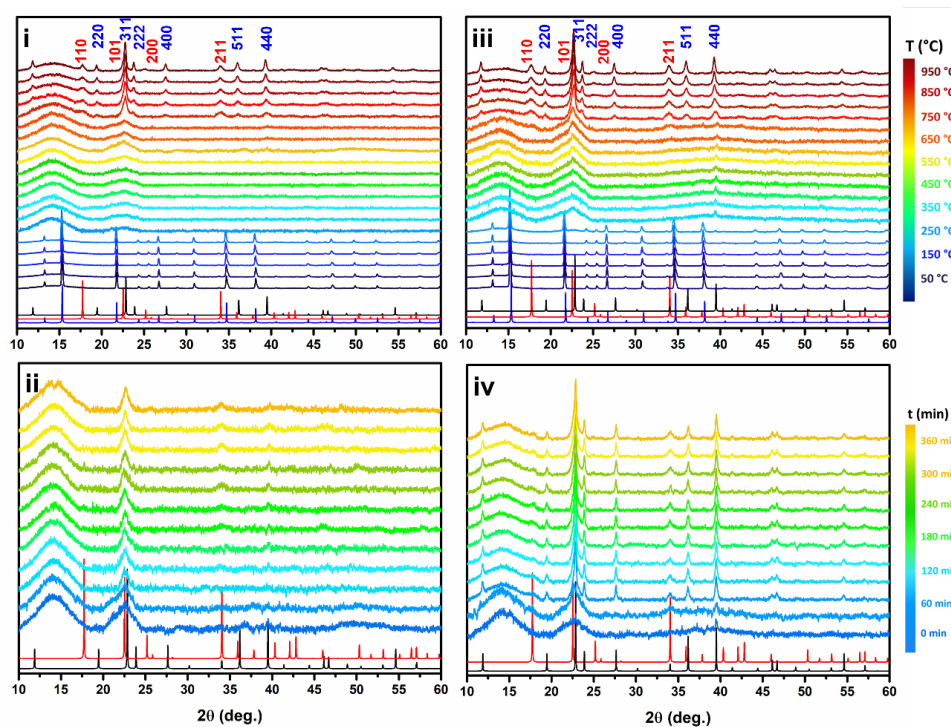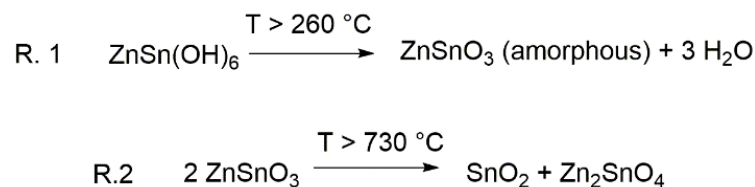
Figure 3. Diffraction data of the particles under the thermal treatments: thermal ramp 30 °C to 950 °C (**i**) under air flux and (**ii**) under vacuum condition; isothermal experiments at 600 °C for 6 (**iii**) under air flux and (**iv**) under vacuum condition. The reference diffraction patterns correspond respectively to blue $ZnSn(OH)_6$ ICSD 27767, red SnO_2 ICSD 9163, and black Zn_2SnO_4 ICSD 11269.

$$\text{R. 1} \quad ZnSn(OH)_6 \xrightarrow{T > 260\ °C} ZnSnO_3 \text{ (amorphous)} + 3\ H_2O$$

$$\text{R.2} \quad 2\ ZnSnO_3 \xrightarrow{T > 730\ °C} SnO_2 + Zn_2SnO_4$$

Scheme 2. Decomposition of $ZnSn(OH)_6$ under thermal treatments.

This analysis clearly shows that the formation of crystalline $ZnSnO_3$, both as lithium niobate or ilmenite type structure, is not observed even as metastable phases during the thermal treatment. Raman measurements, by Ge et al. [25], showed that some contribution of the amorphous phase at a temperature below 320 °C could be attributed to the $ZnSnO_3$ ilmenite type, however, no clear evidence from the XRD patterns were obtained.

To investigate the evolution of the amorphous phase we also monitored the structural transformation at 600 °C for 6 h and under air flux (Figure 3ii). The analysis shows that after 60 min the broad halo of the amorphous phase between 20 and 25 degrees starts shrinking, and at a longer time it contributes to the formation of the 101 reflections, typical of the SnO_2 nanowires. This feature progressively shrinks and after 180 min also 211 reflections can be observed.

2.2. Vacuum Condition

The evolution of the heat-treated material was also investigated under vacuum, and the results are shown in Figure 3iii,iv. The analysis of the diffraction data, from 30 to 950 °C (Figure 3iii), shows similar patterns to the ones obtained under air: it can be deduced that the hydroxide structure is stable until 250–300 °C, and then it decomposes forming an amorphous phase (reaction Scheme 2). As observed for the treatment under air, the formation of the SnO_2 and Zn_2SnO_4 phases can be recognized at temperatures higher than 750 °C, as products of the reaction shown in Scheme 2 (R.2). However, in contrast with

the previous observation, during the thermal treatment under vacuum, the presence of the 440 reflections of the Zn_2SnO_4 phase can be observed immediately after the hydroxide decomposition. To confirm that the vacuum condition favors the formation of the Zn_2SnO_4 phase, the evolution of the structure was investigated at 600 °C for 6 h (see Figure 3iv). As expected, the amorphous phase is rapidly converted to the Zn_2SnO_4 phase, which can be observed already after 30 min due to the presence of the 311, 400, and 440 reflections. For longer times, all the expected reflections of the Zn_2SnO_4 phase can be clearly observed along with the SnO_2 phase.

2.3. Morphology

The SEM and TEM images of the particles treated at different temperatures, shown in Figure 4, evidence that the morphology is strongly affected by the heat treatment, leading to the formation of complex hierarchical structures. Although all the particles retain the original cubic morphology on a micrometric scale, significative modification on the surface scale is observed. Figure 4i (SEM micrograph) shows a detail of the surface of the hydroxide microcrystals before the calcination step. Even though the surface presents some structural defects such as voids, steps, and terraces, most of the particles show the presence of a large flat surface (Figure S5), which can be further clarified by the TEM image in Figure 4v. The morphology and the nucleation conditions suggest that the formation of the $ZnSn(OH)_6$ microcrystals follows a classical crystallization mechanism [47,48]. Indeed, after the nucleation process, hydroxide crystals grow through a layer-by-layer mechanism giving the formation to cubic microcrystals whose crystal habit reflects the crystallographic structure of $ZnSn(OH)_6$ [47].
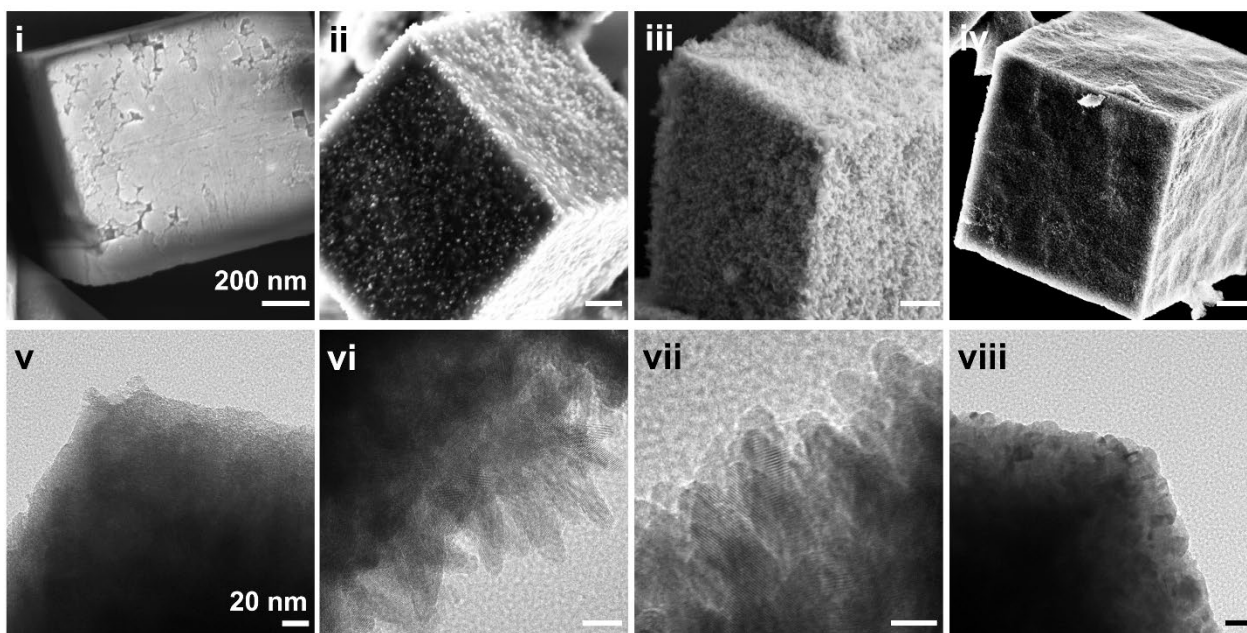

Figure 4. SEM i-iv and TEM v-viii micrographs of the surfaces of particles after different thermal treatments. (**i**,**v**) non treated particles, (**ii**,**vi**) particles treated at 500 °C, (**iii**,**vii**) particles treated at 600 °C and (**iv**,**viii**) particles treated at 750 °C. The scale bars correspond to (**i–iv**) = 200 nm and (**v–viii**) = 20 nm respectively.

Both the samples calcinated at 500 and 600 °C (Figure 4ii,iii) show the presence of cubic microparticles that are covered by a dense layer of nanorods with an average length and thickness of about 50 and 20 nm, respectively (Figure 4vi,vii).

The phase contrast TEM images of the sample calcined at 500 °C (Figure 5i) show that the nanowires are formed by single crystals. The analysis of the lattice fringes allows the identification of the 110 (d spacing = 0.35 nm) and 101 (d spacing = 0.26 nm) planes, typical

of the SnO_2 rutile phase. The identification of the crystalline phase is further supported by SAED analysis (Figure 5ii), which shows a ring pattern that can be related to SnO_2 crystals. These findings suggest that the SnO_2 nanorods do grow from the surface of the amorphous cubic particles along the 101 directions. This behavior also explains the higher intensity of the 101-reflection feature observed in the XRD analysis. Therefore, the heat-treated particles at 500 °C and 600 °C show a peculiar hierarchical morphology composed of amorphous cubes whose surfaces are covered by SnO_2 nanowires.
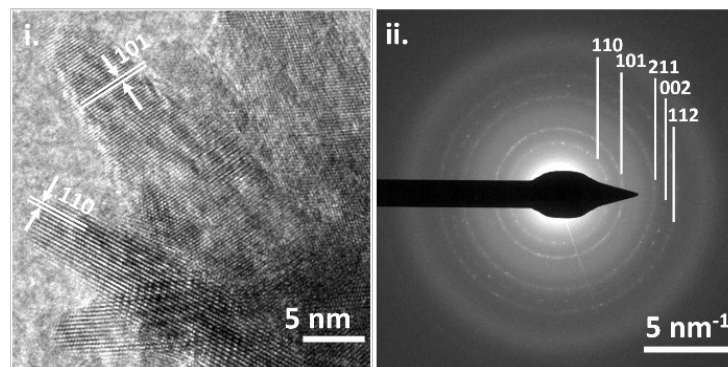

Figure 5. (**i**) phase contrast TEM micrograph of the SnO_2 nanowires structure (scale bar: 5 nm) and (**ii**) SAED analysis scale bar 5 nm^{-1}.

Finally, in contrast with the sample treated at a lower temperature, the morphology of $ZnSn(OH)_6$ microcubes treated at 750 °C does not show the presence of SnO_2 nanowires on the surface (Figure 4iv). Instead, the surface of the cubic microparticles is covered by sintered nanoparticles. This structural feature is further highlighted in the TEM image (Figure 4viii) along with the observation of the diffraction fringes from the nanoparticles confirming their crystallinity (Figure S6). It can be deduced that the nanoparticles correspond to the nanocrystal domine of both the Zn_2SnO_4 and SnO_2 phases. For these samples, a different hierarchical structure compared to low-temperature treated $ZnSn(OH)_6$ can be observed. Indeed, the cubes are formed by a dense arrangement of SnO_2 and Zn_2SnO_4 crystalline nanoparticles which preserves the cubic micrometrical morphology of the original $ZnSn(OH)_6$.

Comparing our morphological results with the literature it emerges that a cubic structure of the $ZnSnO_3$ phase is never obtained [28,29,40]. Indeed, a preferential growth along the 003 or 110 planes for $ZnSnO_3$ has been reported by Datta et al. [29] which led to the formation of a tightly welded nanowire, as also shown by Wang and Wu [28]. The cubic morphology is generally presented for the $ZnSn(OH)_6$ phase before and after thermal treatments [44,45], supporting the hypothesis that the formation of the $ZnSnO_3$ phase cannot be achieved through commonly employed methods.

Figure 6 summarizes the process that affects the structure and morphology of $ZnSn(OH)_6$ microcubes under thermal treatments. In all the investigated conditions, the thermal decomposition of $ZnSn(OH)_6$ microcubes never revealed the formation of crystalline $ZnSnO_3$, but only an amorphous phase. DFT calculations reported by Lee et al. [49] have shown that $ZnSnO_3$ is the less stable phase at ambient pressure and can be synthesized only at a minimum pressure of 5.1 GPa. On the other hand, the mixture of Zn_2SnO_4 and SnO_2 can be obtained at ambient pressure at temperatures above 767 °C. These results agree with our experimental data, supporting the idea that the synthesis of $ZnSnO_3$ needs peculiar requirements (high pressure [26], ion exchange [40], or epitaxial growth from substrates [27,29]) to be achieved.
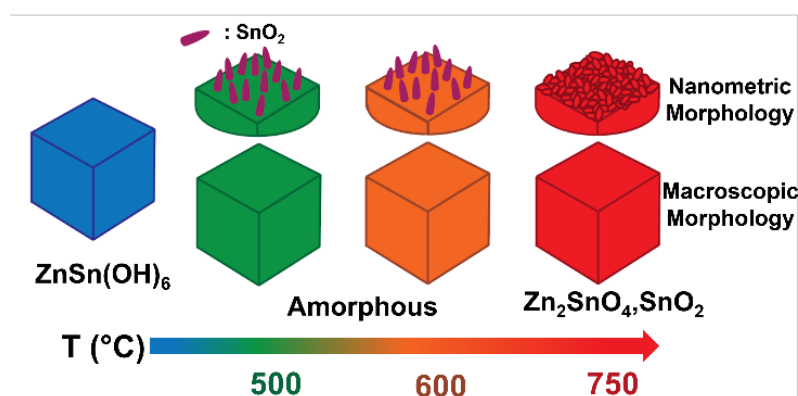
Figure 6. Schematic representation of the evolution of the particle morphology and crystalline structure according to the different calcination temperatures employed.

Additional investigations about $ZnSnO_3$ and the properties of the Zn-Sn-O amorphous phase are still required. Understanding their formation and the chemistry of the defects in the amorphous phase might help identify useful dopants that could promote the formation of the $ZnSnO_3$ metastable phase by low-pressure synthesis. Ion doping may be a potential strategy to expand the range of conditions for the stabilization of the perovskite phase. A large number of observations on the variation of structure and electronical properties in ternary systems, such as ZnO-In_2O_3-SnO_2, are available [50]. Promising results have been indeed obtained by Hoel et al. [51] which showed that the high-pressure synthesis of Zn and Sn co-doped In_2O_3 gives the formation of a polar lithium niobate type structure as suggested by the observation of second harmonic generation. This evidence supports future investigations on the role of ion doping to expand the thermodynamic range for the stabilization of the $ZnSnO_3$ phase.

3. Materials and Methods

3.1. Materials

Zinc acetate (99%), Tin(IV) chloride pentahydrate (99%), and NaOH were purchased from Sigma Aldrich (St. Louis, MO, USA). All the chemicals were employed without further purification.

3.2. ZnSn(OH)$_6$ Preparation and Thermal Treatments

In a typical synthesis, 0.183 g of Zinc acetate (1.0 mmol) and 0.351 g of Tin(IV) chloride pentahydrate (1.0 mmol) are dissolved in 50 mL of distilled water each in two separate beakers. When the solutions become clear, they are poured together in a round bottom flask equipped with a bubble condenser and stirred for 10 min. Then, 50.0 mL of a NaOH solution (0.2 M) is slowly dropped into the round bottom flask; after a few minutes, the solution becomes slightly opaque. The reaction mixture is refluxed at 100 °C in a water bath for 1.0 h under constant stirring, while a white precipitate is formed. The resulting white suspension is centrifuged at 7000 rpm for 5.0 min and the solid is washed first with distilled water, then with an EtOH/H_2O solution, and finally with ethanol. The $ZnSn(OH)_6$ powder is then dried in air at 60 °C overnight. Thermal treatments of the $ZnSn(OH)_6$ phase are performed by firing the powder at 500, 600, 700, 750, and 800 °C for 2 h under an ambient atmosphere (heating rate 5 °C/min). The in-situ phase conversion has been followed through the use of synchrotron radiation, heat treating $ZnSn(OH)_6$ at different temperatures between 30 and 950 °C with a heating rate of 10 °C/min, under air flux or vacuum conditions.

3.3. Structural Characterization

X-ray powder diffraction (XRPD) analysis is performed by means of a Philips diffractometer with a PW 1319 goniometer with Bragg–Brentano geometry. A focusing graphite

monochromator and a proportional counter with a pulse-height discriminator have been used; nickel-filtered Cu Kα radiation and a step-by-step technique have been employed; steps of 0.05° and a collection time of 30 s were used for the acquisition of the data employed in the Rietveld analysis. Temperature-dependent in situ synchrotron radiation X-ray powder diffraction (SR-XRPD) measurements were performed at the MCX line of the ELETTRA Synchrotron Light Laboratories of Trieste, using a 0.30 mm quartz glass capillary as a sample holder and membrane pump for the in-vacuum measurements. TG-DSC (NETZSCH STA 409C) was carried out between 25 and 900 °C with a heating rate of 10 °C/min under an air atmosphere. SEM images were acquired using a Zeiss Sigma VP Field Emission Scanning Electron Microscope (FE-SEM) equipped with an in-lens electrons detector working in high vacuum mode and an EHT voltage of 5 kV. TEM images and SAED patterns were obtained using a ThermoFisher Talos equipped with a field emission gun cathode operated at 200 kV.

4. Conclusions

Our investigation covers a critical analysis of the evolution of $ZnSn(OH)_6$ microcubes under commonly employed thermal treatments for the conversion of these hydroxide micro-crystals into the derivate oxides. We studied the structural modifications that $ZnSn(OH)_6$ cubical microcrystals prepared via reflux condition encounter during the thermal treatment, combining the observations collected by the room temperature X-ray diffraction with an in-situ investigation in dedicated synchrotron experiments. Moreover, we focused our attention on the alterations of the morphological structure of the microcrystals. We noticed that regardless of the preservation of the original cubic shape, the microparticles undergo a complex evolution forming a variety of hierarchical 3D structures, and the final morphology is strongly affected by the specific conditions employed during the post-synthesis calcination step. Indeed, the samples treated at lower temperatures of 500 or 600 °C are characterized by the presence of a dense layer of SnO_2 nanorods on their surface. Instead, the sample treated at 750 °C shows the presence of a packed assembly of SnO_2 and Zn_2SnO_4 nanocrystals. In all the investigated conditions, the thermal decomposition at ambient pressure of $ZnSn(OH)_6$ microcubes never revealed the formation of crystalline $ZnSnO_3$, these results evidences the peculiarities of the synthesis of the zinc stannate system preventing the formation of the perovskite phase under conventional reaction conditions. With this work, we want to stimulate a deep investigation into the origin of piezoelectric properties in these structures to collect fundamental information for the design of novel devices.

Supplementary Materials: The following supporting information can be downloaded at: https://www.mdpi.com/article/10.3390/inorganics10110183/s1, Figure S1: Size length distribution of ZnSn(OH)6 microcubes; Figure S2: Rietveld refinement of ZnSn(OH)6; Figure S3: XRD pattern comparison for product treated at 750 °C with SnO2 and Zn2SnO4; Figure S4: TG-DSC curves performed on ZnSn(OH)6 microcubes; Figure S5: SEM images of ZnSn(OH)6 microcubes, scale bars: (i) 200 nm and (ii) 100 nm; Figure S6: TEM image of the surface of the particles treated at 750 °C, scale bars 10 nm.

Author Contributions: Conceptualization, D.R.-B. and L.B.; methodology, D.R.-B.; software, D.R.-B.; validation, M.B.; formal analysis, L.B.; investigation, D.R.-B.; resources, A.B.; data curation, D.R.-B.; writing—original draft preparation, D.R.-B. and L.B.; writing—review and editing, M.B., P.R., A.S., N.P., and A.B.; visualization, A.B.; supervision, A.B.; project administration, A.S.; funding acquisition, A.B. All authors have read and agreed to the published version of the manuscript.

Data Availability Statement: All the data are available within the manuscript and in the Supplementary Material.

Conflicts of Interest: The authors declare no conflict of interest.

References

1.   Horrocks, A.R.; Anand, S.C. *Handbook of Technical Textiles*, 2nd ed.; Technical Textile Applications; Woodhead: Sawston, UK, 2016; Volume 2, ISBN 9780857090560.

2.   Hosseini, E.S.; Manjakkal, L.; Shakthivel, D.; Dahiya, R. Glycine-Chitosan-Based Flexible Biodegradable Piezoelectric Pressure Sensor. *ACS Appl. Mater. Interfaces* **2020**, *12*, 9008–9016. [CrossRef] [PubMed]

3.   Chen, Z.; Wang, Z.; Li, X.; Lin, Y.; Luo, N.; Long, M.; Zhao, N.; Xu, J.-B. Flexible Piezoelectric-Induced Pressure Sensors for Static Measurements Based on Nanowires/Graphene Heterostructures. *ACS Nano* **2017**, *11*, 4507–4513. [CrossRef]

4.   Zaszczyńska, A.; Gradys, A.; Sajkiewicz, P. Progress in the Applications of Smart Piezoelectric Materials for Medical Devices. *Polymers* **2020**, *12*, 2754. [CrossRef]

5.   Zhang, C.; Fan, Y.; Li, H.; Li, Y.; Zhang, L.; Cao, S.; Kuang, S.; Zhao, Y.; Chen, A.; Zhu, G.; et al. Fully Rollable Lead-Free Poly(Vinylidene Fluoride)-Niobate-Based Nanogenerator with Ultra-Flexible Nano-Network Electrodes. *ACS Nano* **2018**, *12*, 4803–4811. [CrossRef] [PubMed]

6.   Hu, D.; Yao, M.; Fan, Y.; Ma, C.; Fan, M.; Liu, M. Strategies to Achieve High Performance Piezoelectric Nanogenerators. *Nano Energy* **2019**, *55*, 288–304. [CrossRef]

7.   Sezer, N.; Koç, M. A Comprehensive Review on the State-of-the-Art of Piezoelectric Energy Harvesting. *Nano Energy* **2021**, *80*, 105567. [CrossRef]

8.   Mahapatra, S.D.; Mohapatra, P.C.; Aria, A.I.; Christie, G.; Mishra, Y.K.; Hofmann, S.; Thakur, V.K. Piezoelectric Materials for Energy Harvesting and Sensing Applications: Roadmap for Future Smart Materials. *Adv. Sci.* **2021**, *8*, 2100864. [CrossRef] [PubMed]

9.   Niu, X.; Jia, W.; Qian, S.; Zhu, J.; Zhang, J.; Hou, X.; Mu, J.; Geng, W.; Cho, J.; He, J.; et al. High-Performance PZT-Based Stretchable Piezoelectric Nanogenerator. *ACS Sustain. Chem. Eng.* **2019**, *7*, 979–985. [CrossRef]

10.   Kang, M.G.; Jung, W.S.; Kang, C.Y.; Yoon, S.J. Recent Progress on PZT Based Piezoelectric Energy Harvesting Technologies. *Actuators* **2016**, *5*, 5. [CrossRef]

11.   Zhang, S.; Lin, X.; Liu, H.; Yuan, Z.; Huan, Y.; Yuan, X.; Huang, S.; Cheng, X. High-Performance Flexible Piezoelectric Nanogenerator Based on Necklace-like PZT Particle Chains. *Int. J. Energy Res.* **2021**, *45*, 6213–6226. [CrossRef]

12.   Kim, E.J.; Lee, T.G.; Kim, D.S.; Kim, S.W.; Yee, Y.J.; Han, S.H.; Kang, H.W.; Nahm, S. Textured $Pb(Zr,Ti)O_3$-$Pb[(Zn,Ni)_{1/3}Nb_{2/3}]O_3$ Multilayer Ceramics and Their Application to Piezoelectric Actuators. *Appl. Mater. Today* **2020**, *20*, 100695. [CrossRef]

13.   Chen, B.; Li, H.; Tian, W.; Zhou, C. PZT Based Piezoelectric Sensor for Structural Monitoring. *J. Electron. Mater.* **2019**, *48*, 2916–2923. [CrossRef]

14.   Wang, H.S.; Hong, S.K.; Han, J.H.; Jung, Y.H.; Jeong, H.K.; Im, T.H.; Jeong, C.K.; Lee, B.-Y.; Kim, G.; Yoo, C.D.; et al. Biomimetic and Flexible Piezoelectric Mobile Acoustic Sensors with Multiresonant Ultrathin Structures for Machine Learning Biometrics. *Sci. Adv.* **2021**, *7*, 7. [CrossRef] [PubMed]

15.   Koruza, J.; Bell, A.J.; Frömling, T.; Webber, K.G.; Wang, K.; Rödel, J. Requirements for the Transfer of Lead-Free Piezoceramics into Application. *J. Mater.* **2018**, *4*, 13–26. [CrossRef]

16.   Chen, X.; Sun, J.; Guo, B.; Wang, Y.; Yu, S.; Wang, W.; Bai, J. Effect of the Particle Size on the Performance of $BaTiO_3$ Piezoelectric Ceramics Produced by Additive Manufacturing. *Ceram. Int.* **2022**, *48*, 1285–1292. [CrossRef]

17.   Jiang, J.; Tu, S.; Fu, R.; Li, J.; Hu, F.; Yan, B.; Gu, Y.; Chen, S. Flexible Piezoelectric Pressure Tactile Sensor Based on Electrospun $BaTiO_3$/Poly(Vinylidene Fluoride) Nanocomposite Membrane. *ACS Appl Mater Interfaces* **2020**, *12*, 33989–33998. [CrossRef] [PubMed]

18.   Gao, J.; Xue, D.; Liu, W.; Zhou, C.; Ren, X. Recent Progress on $BaTiO_3$-Based Piezoelectric Ceramics for Actuator Applications. *Actuators* **2017**, *6*, 24. [CrossRef]

19.   Branzi, L.; Back, M.; Cortelletti, P.; Pinna, N.; Benedetti, A.; Speghini, A. Sodium Niobate Based Hierarchical 3D Perovskite Nanoparticle Clusters. *Dalton Trans.* **2020**, *49*, 15195–15203. [CrossRef] [PubMed]

20.   Ji, S.; Liu, H.; Sang, Y.; Liu, W.; Yu, G.; Leng, Y. Synthesis, Structure, and Piezoelectric Properties of Ferroelectric and Antiferroelectric $NaNbO_3$ Nanostructures. *CrystEngComm* **2014**, *16*, 7598–7604. [CrossRef]

21.   Jung, J.H.; Lee, M.; Hong, J.; Ding, Y.; Chen, C.Y.; Chou, L.J.; Wang, Z.L. Lead-Free $NaNbO_3$ Nanowires for a High Output Piezoelectric Nanogenerator. *ACS Nano* **2011**, *5*, 10041–10046. [CrossRef]

22.   Xu, M.; Kang, H.; Guan, L.; Li, H.; Zhang, M. Facile Fabrication of a Flexible $LiNbO_3$ Piezoelectric Sensor through Hot Pressing for Biomechanical Monitoring. *ACS Appl. Mater. Interfaces* **2017**, *9*, 34687–34695. [CrossRef]

23. Clementi, G.; Lombardi, G.; Margueron, S.; Suarez, M.A.; Lebrasseur, E.; Ballandras, S.; Imbaud, J.; Lardet-Vieudrin, F.; Gauthier-Manuel, L.; Dulmet, B.; et al. LiNbO₃ Films—A Low-Cost Alternative Lead-Free Piezoelectric Material for Vibrational Energy Harvesters. *Mech. Syst. Signal Process.* **2021**, *149*, 107171. [CrossRef]

24. Kil Yun, B.; Keun Park, Y.; Lee, M.; Lee, N.; Jo, W.; Lee, S.; Hoon Jung, J. Lead-Free LiNbO₃ Nanowire-Based Nanocomposite for Piezoelectric Power Generation. *Nanoscale Res. Lett.* **2014**, *9*, 4.

25. Ge, Q.; Liu, C.; Zhao, Y.; Wang, N.; Zhang, X.; Feng, C.; Zhang, S.; Wang, H.; Jiang, W.; Liu, S.; et al. Phase Evolution in Preparing ZnSnO₃ Powders by Precipitation Method. *Appl. Phys. A* **2021**, *127*, 89. [CrossRef]

26. Inaguma, Y.; Yoshida, M.; Katsumata, T. A Polar Oxide ZnSnO₃ with a LiNbO₃-Type Structure. *J. Am. Chem. Soc.* **2008**, *130*, 6704–6705. [CrossRef]

27. Jong, Y.S.; Lee, G.; Jo, M.H.; Kim, H.; Jang, H.M.; Shin, Y.H. Heteroepitaxial Ferroelectric ZnSnO₃ Thin Film. *J. Am. Chem. Soc.* **2009**, *131*, 8386–8387. [CrossRef]

28. Wang, Y.C.; Wu, J.M. Effect of Controlled Oxygen Vacancy on H₂-Production through the Piezocatalysis and Piezophototronics of Ferroelectric R3C ZnSnO₃ Nanowires. *Adv. Funct. Mater.* **2020**, *30*, 1907619. [CrossRef]

29. Datta, A.; Mukherjee, D.; Kons, C.; Witanachchi, S.; Mukherjee, P. Evidence of Superior Ferroelectricity in Structurally Welded ZnSnO₃ Nanowire Arrays. *Small* **2014**, *10*, 4093–4099. [CrossRef]

30. Cao, Y.; Jia, D.; Zhou, J.; Sun, Y. Simple Solid-State Chemical Synthesis of ZnSnO₃ Nanocubes and Their Application as Gas Sensors. *Eur. J. Inorg. Chem.* **2009**, *2009*, 4105–4109. [CrossRef]

31. Song, P.; Wang, Q.; Yang, Z. Biomorphic Synthesis of ZnSnO₃ Hollow Fibers for Gas Sensing Application. *Sens. Actuators B Chem.* **2011**, *156*, 983–989. [CrossRef]

32. Para, T.A.; Reshi, H.A.; Shelke, V. Synthesis of ZnSnO₃ Nanostructure by Sol Gel Method. *AIP Conf. Proc.* **2016**, *1731*, 050002.

33. Paria, S.; Karan, S.K.; Bera, R.; Das, A.K.; Maitra, A.; Khatua, B.B. A Facile Approach to Develop a Highly Stretchable PVC/ZnSnO₃ Piezoelectric Nanogenerator with High Output Power Generation for Powering Portable Electronic Devices. *Ind. Eng. Chem. Res.* **2016**, *55*, 10671–10680. [CrossRef]

34. Lee, K.Y.; Kim, D.; Lee, J.H.; Kim, T.Y.; Gupta, M.K.; Kim, S.W. Unidirectional High-Power Generation via Stress-Induced Dipole Alignment from ZnSnO₃ Nanocubes/Polymer Hybrid Piezoelectric Nanogenerator. *Adv. Funct. Mater.* **2014**, *24*, 37–43. [CrossRef]

35. Ul Haq, M.; Zhang, Z.; Chen, X.; Rahman, N.; Khan, S.; Khatoon, R.; Hassan, S.S.; Ye, Z.; Zhu, L. A Two-Step Synthesis of Microsphere-Decorated Fibers Based on NiO/ZnSnO₃ Composites towards Superior Ethanol Sensitivity Performance. *J. Alloys Compd.* **2019**, *777*, 73–83. [CrossRef]

36. Chen, Q.; Wang, Y.; Wang, M.; Ma, S.; Wang, P.; Zhang, G.; Chen, W.; Jiao, H.; Liu, L.; Xu, X. Enhanced Acetone Sensor Based on Au Functionalized In-Doped ZnSnO₃ Nanofibers Synthesized by Electrospinning Method. *J. Colloid Interface Sci.* **2019**, *543*, 285–299. [CrossRef] [PubMed]

37. Sasmal, A.; Medda, S.K.; Devi, P.S.; Sen, S. Nano-ZnO Decorated ZnSnO₃ as Efficient Fillers in PVDF Matrixes: Toward Simultaneous Enhancement of Energy Storage Density and Efficiency and Improved Energy Harvesting Activity. *Nanoscale* **2020**, *12*, 20908–20921. [CrossRef]

38. Guo, R.; Guo, Y.; Duan, H.; Li, H.; Liu, H. Synthesis of Orthorhombic Perovskite-Type ZnSnO₃ Single-Crystal Nanoplates and Their Application in Energy Harvesting. *ACS Appl. Mater. Interfaces* **2017**, *9*, 8271–8279. [CrossRef]

39. Wang, G.; Xi, Y.; Xuan, H.; Liu, R.; Chen, X.; Cheng, L. Hybrid Nanogenerators Based on Triboelectrification of a Dielectric Composite Made of Lead-Free ZnSnO₃ Nanocubes. *Nano Energy* **2015**, *18*, 28–36. [CrossRef]

40. Kovacheva, D.; Petrov, K. Preparation of Crystalline ZnSnO from Li SnO by Low-3 2 3 Temperature Ion Exchange. *Solid State Ion* **1998**, *109*, 327–332. [CrossRef]

41. Kholkin, A.L.; Pertsev, N.A.; Goltsev, A.V. *Piezoelectricity and Crystal Symmetry*; Springer: Boston, MA, USA, 2008.

42. Park, D.-S.; Hadad, M.; Riemer, L.M.; Ignatans, R.; Spirito, D.; Esposito, V.; Tileli, V.; Gauquelin, N.; Chezganov, D.; Jannis, D.; et al. Induced Giant Piezoelectricity in Centrosymmetric Oxides. *Science* **2022**, *375*, 653–657. [CrossRef]

43. Yang, M.M.; Luo, Z.D.; Mi, Z.; Zhao, J.; Alexe, M. Piezoelectric and Pyroelectric Effects Induced by Interface Polar Symmetry. *Nature* **2020**, *584*, 377–381. [CrossRef] [PubMed]

44. Lu, J.; Xie, Y.; Luo, F.; Fu, H.; Huang, X.; Liu, Y.; Liu, H. Heterostructures of Mesoporous Hollow Zn₂SnO₄/SnO₂ Microboxes for High-Performance Acetone Sensors. *J. Alloys Compd.* **2020**, *844*, 155788. [CrossRef]

45. Wang, K.; Liu, D.; Deng, P.; Liu, L.; Lu, S.; Sun, Z.; Ma, Y.; Wang, Y.; Li, M.; Xia, B.Y.; et al. Band Alignment in Zn₂SnO₄/SnO₂ Heterostructure Enabling Efficient CO₂ Electrochemical Reduction. *Nano Energy* **2019**, *64*, 103954. [CrossRef]

46. Zhang, R.; Ma, S.Y.; Zhang, Q.X.; Zhu, K.M.; Tie, Y.; Pei, S.T.; Wang, B.J.; Zhang, J.L. Highly Sensitive Formaldehyde Gas Sensors Based on Ag Doped Zn₂SnO₄/SnO₂ Hollow Nanospheres. *Mater. Lett.* **2019**, *254*, 178–181. [CrossRef]

47. Sunagawa, I. *Crystals: Growth, Morphology, and Perfection*; Cambridge University Press: Cambridge, UK, 2005.

48. Cölfen, H.; Antonietti, M. *Mesocrystal and Non-Classical Crystallization*; John Wiley & Sons: Hoboken, NJ, USA, 2008.

49. Lee, J.; Lee, S.C.; Hwang, C.S.; Choi, J.H. Thermodynamic Stability of Various Phases of Zinc Tin Oxides from Ab Initio Calculations. *J. Mater. Chem. C Mater.* **2013**, *1*, 6364–6374. [CrossRef]

50. Hoel, C.A.; Mason, T.O.; Gaillard, J.F.; Poeppelmeier, K.R. Transparent Conducting Oxides in the ZnO-In₂O₃-SnO₂ System. *Chem. Mater.* **2010**, *22*, 3569–3579. [CrossRef]

51. Hoel, C.A.; Amores, J.M.G.; Morán, E.; Álario-Franco, M.A.; Gaillard, J.F.; Poeppelmeier, K.R. High-Pressure Synthesis and Local Structure of Corundum-Type In 2-2xZnxSnxO₃ (x ≤ 0.7). *J. Am. Chem. Soc.* **2010**, *132*, 16479–16487. [CrossRef]